

Wetting dynamics and particle deposition for an evaporating colloidal drop: A lattice Boltzmann study

Abhijit S. Joshi^{*} and Ying Sun[†]*Drexel University, Philadelphia, Pennsylvania 19104, USA*

(Received 17 January 2010; revised manuscript received 6 August 2010; published 7 October 2010)

A three-dimensional lattice Boltzmann method (LBM) has been developed for multiphase (liquid and vapor) flows with solid particles suspended within the liquid phases. The method generalizes our recent two-dimensional model [A. Joshi and Y. Sun, *Phys. Rev. E* **79**, 066703 (2009)] to three dimensions, extends the implicit scheme presented therein to include interparticle forces and introduces an evaporation model to simulate drying of the colloidal drop. The LBM is used to examine the dynamical wetting behavior of drops containing suspended solid particles on homogeneous and patterned substrates. The influence of the particle volume fraction and particle size on the drop spreading dynamics is studied as is the final deposition of suspended particles on the substrate after the carrier liquid evaporates. The final particle deposition can be controlled by substrate patterning, adjusting the substrate surface energies and by the rate of evaporation. Some of the envisioned applications of the model are to develop a fundamental understanding of colloidal drop dynamics, predict particle deposition during inkjet printing of functional materials and to simulate the drying of liquids in porous media.

DOI: [10.1103/PhysRevE.82.041401](https://doi.org/10.1103/PhysRevE.82.041401)

PACS number(s): 83.80.Hj, 05.20.Dd, 68.03.-g, 68.08.Bc

I. INTRODUCTION

The transient behavior of a drop or film of liquid after it contacts a solid surface is typically referred to as wetting dynamics and while this is a very commonly observed phenomenon in everyday life, it plays an important role in many technological processes (e.g., surface coating and painting, lubrication, oil recovery from porous rocks, inkjet printing) and in biological systems like self-cleaning plant leaves. These phenomena have been extensively studied and a recent review can be found in Bonn *et al.* [1]. The simplest possible setting in which to study wetting dynamics is when a drop of pure liquid contacts a flat, rigid and nonporous substrate. It is well known that capillary forces cause such a drop to minimize its total energy and that the interface eventually attains a stable equilibrium position in the shape of a spherical cap (if gravity is negligible).

For an ideally smooth surface, the interface forms a well-defined equilibrium contact angle θ_{eq} with the solid surface, which can be obtained using Young's relationship. If $\theta_{eq} < 90^\circ$, the substrate has a high affinity for the liquid phase (hydrophilic) and when $\theta_{eq} > 90^\circ$, the substrate is hydrophobic. The case where $\theta_{eq} = 90^\circ$ is often referred to as *neutral wetting*. Note that these definitions can also be applicable to solid particles in equilibrium at the liquid-air interface. For morphologically and/or chemically heterogeneous surfaces, it has been observed experimentally that the measured (static) contact angle θ_m depends on the spreading history of the drop and can deviate from θ_{eq} . Thus, θ_m can be anywhere between the *static advancing contact angle* θ_a (the angle when the contact line is stationary but is just about to advance in the direction of the air) and the *static receding contact angle* θ_r (the angle formed when the contact line is

stationary but about to start receding toward the liquid side). Typically, $\theta_r < \theta_{eq} < \theta_a$ and $\theta_r < \theta_m < \theta_a$. The difference $\theta_a - \theta_r$ is referred to as *contact angle hysteresis* and depends on the characteristics of the surface. The transient evolution of the contact angle from the moment the drop touches the substrate until it attains an equilibrium position has been investigated by several researchers, both experimentally [2,3] and using numerical modeling [4–7]. The instantaneous contact angle during this transient evolution is referred to as the *dynamic contact angle* θ_d , and this is typically a function of the contact line velocity.

When suspended solid particles are present in the liquid drop, the wetting dynamics described above becomes considerably more complex and is influenced by a large number of additional parameters. Some of these parameters are the particle volume fraction in the liquid drop, particle size and wetting properties of the particle surface. When the size of suspended particles falls below 1 micron, the suspension is usually referred to as a colloid [8]. At this scale, random bombardment on the suspended particle from molecules present in the continuous liquid phase lead to the well-known phenomenon of Brownian motion. In addition to Brownian motion, colloidal particles also interact directly via DLVO forces [9–11]. There have been very few studies in the literature that model the wetting dynamics of drops containing a uniform distribution of finite-sized suspended particles, colloidal or otherwise. Nicolas [12] experimentally studied the impact, spreading and breakup of nonevaporating liquid drops containing density-matched (neutrally buoyant) solid particles. Using an effective viscosity model for the drop, it was found that the spreading factor scales as $Re^{1/4}$ and a uniform particle distribution in the spread drop is observed for $Re < 800$. Some particle clusters were also observed, indicating that the interaction of suspended particles with the liquid-air interface might play a role in the spreading dynamics. Another recent investigation [13] used a two-dimensional (2D) numerical model to simulate capillary

^{*}joshi1974@gmail.com[†]ysun@coe.drexel.edu

spreading of a liquid drop with suspended solid particles. Qualitative agreements were reached with Ref. [12] regarding the smaller spreading factors for drops with suspended particles and this was attributed to the increase in the effective viscosity. However, the authors did not include inertial terms in their model, so their results are restricted to the Stokes flow regime.

If the liquid phase in a colloidal drop is evaporating, the wetting dynamics and evaporation occur simultaneously and this eventually leads to the deposition of the suspended particles on the substrate. An important example of such a process is inkjet printed particulate suspension drops for printable electronics fabrication [14]. The fundamental physical processes during printing of functional materials (with electrical, optical, chemical, biological, or structural functionalities) can be separated into two stages—(1) drop impact and spreading and (2) evaporation of the carrier liquid phase leading to deposition of suspended particles. The impact stage involves rapid drop deformation, spreading to a maximum diameter followed by minor oscillations or complete rebound, depending on the surface energy of the substrate [15]. The physical mechanisms during the evaporation stage are still the topics of much debate. For example, evaporation of sessile colloidal drops sometimes leads to the “coffee-ring” effect, commonly seen when a drop of coffee dries out. Deegan and co-workers [16–18] explained these ringlike deposits based on the pinning of the contact line and a replenishing flow of the liquid toward the contact line due to evaporation. Hu and Larson [19] concluded that in addition to a pinned contact line, obtaining coffee-ring deposits also require a suppression of Marangoni flow inside the liquid drop.

In the absence of suspended particles, pinning of the contact line is usually attributed to geometrical or chemical heterogeneities of the substrate [20,21]. For evaporating, colloidal drops, pinning may be reinforced by particles jamming the contact line [17]. Kim *et al.* [22] have identified three distinct stages in the evaporation of a liquid drop: the constant contact area mode (pinned contact line, decreasing contact angle), constant contact angle mode (moving contact line) and mixed mode. However, the precise role of thermal gradients, suspended particles and surface heterogeneities on the pinning of the contact line during these various evaporation modes is still not very clear. Perelaer *et al.* [23] examined the particle deposition for inkjet printed drops containing silica microparticles for a range of particle sizes and concluded that the final particle deposit after drop evaporation is a function of the suspended particle size and the equilibrium contact angle of the liquid phase on the substrate. The volume fraction of particles (prior to evaporation) can also influence the final deposition [24,25]. Some recent studies [26–28] use traditional Navier-Stokes equations and mass transfer models to simulate evaporation of a colloidal drop and the subsequent particle deposition, but these approaches do not incorporate finite sized solid particles in the liquid phase and the suspended particle phase is simulated via a passively advected concentration field instead. This type of approach can be useful to obtain macroscopic predictions about particle deposition but does not allow a two-way coupling between the particles and the carrier fluid, where the

fluid flow field is influenced by the presence of the suspended particles and vice-versa. Thus, these models are not suitable for dense suspensions or at the late stages of evaporation when the effects of finite particle size become important.

The primary motivation and ultimate goal of our modeling effort is to develop a fundamental understanding of the physical mechanisms during printing of functional materials using colloidal inks [29,30]. Apart from printed functional materials and the related issue of drop formation in inkjet nozzles [31], the model developed here can also be useful to simulate the flow of particulate slurries [32–36]. Many questions like whether one can define an effective viscosity for suspensions (colloidal or otherwise) remain unanswered [37] and mathematical modeling of such processes can play an important role in clarifying the impact of various parameters like the volume fraction of the suspended solids, viscosity of the carrier liquid phase, adhesive forces between the suspended particles and the fluid and interparticle forces. Some of the simplifying assumptions made in this study are the following:

- (1) The colloidal drop evaporating in air is approximated by a single component multiphase system consisting of a liquid phase (containing solid particles) in equilibrium with its own vapor phase.
- (2) The liquid drop (with or without suspended solid particles) and the surrounding vapor phase are both incompressible and Newtonian.
- (3) The flow during drop spreading is dominated by interfacial or capillary forces.
- (4) When present, evaporation is driven by a reduction in vapor pressure above the liquid drop.
- (5) Suspended particles are not affected by Brownian motion and are not electrically charged.
- (6) Attractive (van der Waals) and repulsive (electrostatic) forces between suspended particles, based on the DLVO theory [9–11], are not considered.
- (7) Gravitational force is assumed to be negligible in comparison with the interfacial forces (zero Bond number).
- (8) Suspended particles and the substrate are perfectly smooth and rigid. All suspended particles are spherical in shape.
- (9) Drop spreading and evaporation takes place under isothermal conditions. Heat transfer is not considered and the latent heat of evaporation is not included in the model.

Prior numerical models used for this class of problems include Stokesian dynamics [38], finite-difference schemes [39,40], the boundary element method (BEM) [41,42], the finite-element method (FEM) [43,44] and the lattice Boltzmann method (LBM) for particle suspensions [45–53]. However, most of these approaches are restricted to suspensions in a single-phase fluid. Over the past two decades, the LBM has also emerged as a powerful tool to investigate multiphase flows [54–59]. The LBM has been used to model drop impact dynamics on a fixed, homogeneous substrate [7] and for studying the motion of liquid drops on corrugated [60], superhydrophobic and patterned substrates [61–63]. Combining and suitably modifying key ideas from LBM multiphase models and LBM particle suspension models can lead to novel schemes [64–67] for simulating the dynamics of liquid

drops containing suspended particles in a computationally efficient manner. In the present work, we extend the 2D multiphase suspension model of Joshi and Sun [67] to 3D and simulate the dynamics of a liquid-vapor system, where the liquid phase is typically in the form of a drop contacting a substrate and the drop contains suspended solid particles that are spherical in shape. As demonstrated in subsequent sections, the present LBM model has the ability to simulate the dynamics of a liquid drop containing suspended particles as it spreads and evaporates on various kinds of substrates. Once the carrier liquid evaporates, the model also predicts the arrangement of the suspended particles on the substrate.

The remainder of the paper is organized as follows. Section II gives a brief summary of the LBM model including how we model evaporation. Section III describes validation of the multiphase model against prior experimental results and then goes on to describe wetting dynamics of drops with suspended particles with and without evaporation. The main conclusions emerging from this study are summarized in Sec. IV.

II. LATTICE BOLTZMANN MODEL

The schematic of the problem that is simulated in this work using the LBM is shown in Fig. 1(a). A liquid phase (drop) containing suspended solid particles is in equilibrium with its vapor phase and contacts a solid substrate at the bottom of the domain. Periodic boundary conditions are used for the faces perpendicular to the x and y axes. At the top boundary, the vapor phase is assigned a fixed density value (equal to the equilibrium density of the vapor) and a fixed *outflow* velocity. This outflow velocity can be used to control the rate of evaporation of the liquid drop. Note that evaporation takes place at a constant temperature and the effects of latent heat are neglected in the present setup. Suspended solid particles interact with the surrounding fluid via hydrodynamic and adhesive forces, but if they come too close to each other or to the substrate, interparticle forces are activated. Figure 1(b) shows three particles whose actual boundary is indicated by solid lines. Each particle has a *comfort zone* indicated by the shaded annular region and whose boundary is indicated by a dashed line. If particles intrude into each others comfort zones (or the comfort zone of the substrate), interparticle forces that act directly between pairs of particles (along the straight line joining their respective centers) or between the substrate and the particle (acting in a direction normal to the substrate) are activated. Separately, adhesive forces between the particle surface and surrounding fluid determine the equilibrium position of particles on the liquid-vapor interface.

The LBM model used in this work is very closely related to and an extension of our multiphase suspension model [67]. Unlike single-phase LBM models of suspended particles, capillary forces between the suspended particles and the fluid can be accounted for in our model. This allows us to simulate preferential wetting of the suspended particles to either the liquid or the vapor phase, similar to earlier work for multicomponent models [65,68]. We have extended the model in Ref. [67] to 3D and extended the implicit scheme

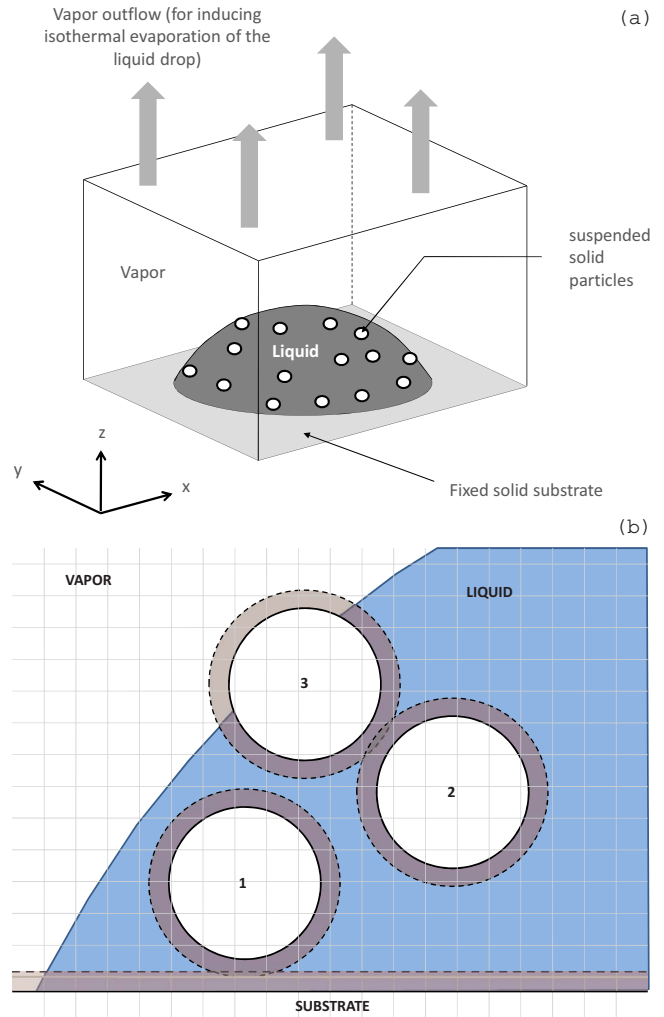


FIG. 1. (Color online) (a) Evaporation of a liquid drop containing suspended particles. The liquid phase is surrounded by and in equilibrium with its vapor phase. The drop rests on a geometrically smooth and fixed solid substrate. (b) Suspended particles are present inside the liquid phase and may be present on the liquid-vapor interface. Interparticle forces are activated when a pair of particles gets too close to each other or to the fixed substrate. In this case, particle 1 is directly influenced by the substrate, and particles 2 and 3 are directly influenced by each other.

discussed therein to include interparticle forces (lubrication forces and Hookean repulsive forces). Note that the rotational dynamics of suspended particles is fully accounted for in the present model. Because the extension to 3D is very straightforward, the details of the multiphase model and the particle suspension model from Ref. [67] are not repeated here, and only a brief overview is given. The implicit scheme used for updating linear and angular velocities of suspended particles is discussed in Appendix A and details about the parallel performance of the LBM model are discussed in Appendix B

The LBM simulates fluid flow on a discrete lattice with equally spaced nodes along the x , y , and z directions. The primary dependent variables at each node are the particle velocity distribution functions (PDFs) along different lattice directions (α). The PDF along a certain direction represents

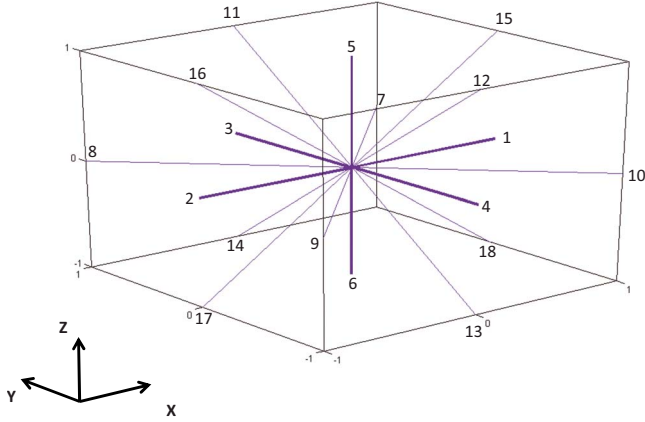


FIG. 2. (Color online) D3Q19 velocity model used in the LBM showing the numbering scheme for neighboring nodes. The discrete velocities \mathbf{e}_α are defined from the origin $(0,0,0)$ to each of these neighboring nodes. Note that $\mathbf{e}_0=(0,0,0)$.

the number of fluid particles moving in that direction at that time and is indicated by f_α . Macroscopic quantities like the fluid density ρ and velocity \mathbf{u} can be calculated by taking moments of these PDFs. The transport of these PDFs along a finite number of discrete lattice directions and their interactions via suitably designed collision terms can effectively reproduce the dynamics of the Navier-Stokes equations. The discrete velocities \mathbf{e}_α depend on the particular velocity model used and we use the D3Q19 model that has 19 velocity directions ($\alpha=0$ to 18) at a given lattice point, as depicted in Fig. 2.

At any lattice node \mathbf{x} , the evolution of the PDF with time t is governed by the lattice Boltzmann equation, given by

$$f_\alpha(\mathbf{x} + \mathbf{e}_\alpha, t + 1) = f_\alpha(\mathbf{x}, t) - \left[\frac{f_\alpha(\mathbf{x}, t) - f_\alpha^{eq}[\rho(\mathbf{x}, t), \mathbf{u}(\mathbf{x}, t)]}{\tau} \right] + f_\alpha^{eq}[\rho(\mathbf{x}, t), \tilde{\mathbf{u}}(\mathbf{x}, t)] - f_\alpha^{eq}[\rho(\mathbf{x}, t), \mathbf{u}(\mathbf{x}, t)]. \quad (1)$$

The right-hand side in Eq. (1) represents the collision step and equating the right-hand side to the left hand side represents the streaming step. All equations in this work are presented in *lattice units*, where the lattice spacing along the x and y axes and the time step are all unity ($\Delta x = \Delta y = \Delta t = 1$). The relaxation time in Eq. (1) controls the kinematic viscosity ν of the lattice Boltzmann fluid via the relationship $\nu = (2\tau - 1)/6$. The last two terms in Eq. (1) are the result of using the exact difference method (EDM) introduced by Kupershtokh and Medvedev [69]. The EDM ensures that the density ratio between the liquid and vapor phases is not affected when the relaxation time τ is different than unity or when different values of τ are used in the liquid and vapor phases. As discussed in Ref. [67], the modified velocity $\tilde{\mathbf{u}}$ in Eq. (1) accounts for adhesive and cohesive interactions between fluid particles and $\tilde{\mathbf{u}}$ is calculated using

$$\tilde{\mathbf{u}} = \mathbf{u} + \frac{1}{\rho} (\mathbf{F}_{cohesive} + \mathbf{F}_{adhesive}). \quad (2)$$

The multiphase dynamics in the LBM is simulated via the interaction model of Shan and Chen [55]. The cohesive force

$\mathbf{F}_{cohesive}$ at location \mathbf{x} arises because of the attraction between fluid particles at \mathbf{x} and fluid particles at neighboring locations $\mathbf{x} + \mathbf{e}_\alpha$. This attraction is proportional to the effective density [55], $\Psi(\mathbf{x}) = \Psi[\rho(\mathbf{x})] = 1 - \exp(-\rho)$, at interacting nodes and is calculated using

$$\mathbf{F}_{cohesive}(\mathbf{x}) = - \sum_{\alpha=1}^{18} G_\alpha^{fluid-fluid} \Psi(\mathbf{x}) \Psi(\mathbf{x} + \mathbf{e}_\alpha) \mathbf{e}_\alpha. \quad (3)$$

For the D3Q19 velocity model, $G_\alpha^{fluid-fluid} = g_f$ for $\alpha=1$ to 6 and $G_\alpha^{fluid-fluid} = g_f/2$ for $\alpha=7$ to 18. The parameter g_f determines the density ratio between the liquid and vapor phase. The adhesive force is given by

$$\mathbf{F}_{adhesive}(\mathbf{x}) = - \sum_{\alpha=1}^{18} G_\alpha^{fluid-solid} \rho(\mathbf{x}) \rho_s(\mathbf{x} + \mathbf{e}_\alpha) \mathbf{e}_\alpha, \quad (4)$$

where $G_\alpha^{fluid-solid} = g_w$ for $\alpha=1$ to 6 and $G_\alpha^{fluid-solid} = g_w/2$ for $\alpha=7$ to 18. The function $\rho_s(\mathbf{x} + \mathbf{e}_\alpha) = 1$ if the location $\mathbf{x} + \mathbf{e}_\alpha$ corresponds to a solid node (or a fluid node inside suspended particles) and $\rho_s(\mathbf{x} + \mathbf{e}_\alpha) = 0$ otherwise. As discussed in Ref. [67], we use the parameter g_w both to control the contact angle between the liquid and the substrate and to tune the wetting behavior of the suspended particles at the liquid-vapor interface.

For simplicity, the suspended particles are spherical in shape and the location of each particle, the particle radii and the linear and angular velocities are specified as part of the initial conditions. In addition, all the particles are similar in size for the simulations reported here. To allow the particle to interact with the liquid and vapor phase on the LBM lattice, nodes inside and outside the particle are identified. Boundary nodes are located half way between fluid nodes inside the particle and external fluid nodes. As the particle moves, this mapping is updated. Initially, nodes lying in the liquid phase are assigned the liquid density and nodes in the vapor phase are assigned the vapor density, corresponding to the value of the cohesive force parameter g_f . Note that the fluid phase is present at all nodes in the domain, except fixed solid nodes, if any. The fluid velocity is initially set to zero at all nodes unless otherwise specified. Forces and torques on each suspended particle are calculated at each time step based on the momentum transferred to them from the surrounding (external) fluid. Particle positions are then updated using Newton's second law. In addition to momentum transferred because of fluid motion, we include adhesive forces between the particle and the fluid and interparticle forces that prevent particles from overlapping [67].

There are two types of interparticle forces in the present model. The first is the relative-velocity dependent lubrication force F_L between two smooth and rigid spheres of radii R , given by [48]

$$F_L = \begin{cases} 6\pi\mu V_{rel} \frac{1}{4} \left(\frac{1}{h} - \frac{1}{h_c} \right), & h < h_c \\ 0, & h \geq h_c, \end{cases} \quad (5)$$

where μ is the viscosity of the liquid present in between the particles, V_{rel} is the relative velocity of approach, h is the gap between the particle surfaces and h_c is the critical separation

below which this force is active. This force acts on both particles along the line joining their centers and can be repulsive or attractive depending on whether the particles are moving toward or away from each other, respectively. An important consequence of the force in Eq. (5) is the irreversible clustering together of suspended particles once they are closer than the critical separation distance h_c and a tendency to resist separation [38,70–72]. In lieu of the cluster-implicit update scheme [48], we use an explicit update scheme for incorporating lubrication forces, where updating the velocity of each suspended particle is done independently. The typical values for h_c in our simulations range from 1.1 to 2.1 lattice units.

In some cases, the lubrication force is not sufficient to prevent a pair of particles from overlapping and additional repulsive forces are often introduced [73]. In our work, a velocity-independent repulsive force F_H is introduced between particles when the gap between particle surfaces h falls below a critical spacing δ . This force also acts along the line joining the centers of interacting particle pairs and is given by [74]

$$F_H = \begin{cases} 0, & h \geq \delta \\ -F_0 \left(1 - \frac{h}{\delta}\right), & h < \delta. \end{cases} \quad (6)$$

The constants F_0 and δ can be adjusted in order to tune this repulsive force. We observe that properly tuning this repulsive force is critical for stable calculations, especially at high particle volume fractions.

Because of its complex implementation, many LBM suspension models ignore the lubrication forces entirely [75–77] and rely solely on a velocity-independent repulsive force between suspended particles. As discussed in Ref. [75], this approach can be justified if the particles are prevented from coming very close to each other by appropriate repulsive forces. Such a repulsive force is often present in colloidal systems in the form of a screened electrostatic repulsion, which is one part of the DLVO forces. We use $F_0=40$ and $\delta=0.05$ for the simulations reported in this manuscript, which were chosen by trial and error and led to stable computations for the cases considered. Once the proper parameter space for stable simulations was identified, the sensitivity of the results to changes in the above parameter values (h_c , δ and F_0) was not very significant in our simulations. It must be noted that the issue of interparticle forces is often treated in an *ad-hoc* manner within the LBM community and its implications on the results are not explored in detail as long as the basic purpose of preventing particle overlap is achieved.

To model evaporation in the Shan and Chen based two-phase LBM, we assigned a fixed velocity u_z at the top of the domain via *equilibrium forcing*. All the particle distribution functions (PDFs) at the topmost plane of the domain were forced to be equal to the equilibrium PDF values corresponding to the vapor density and the prescribed outflow velocity. Physically, this evaporation mechanism can be understood in the following manner. First, because the vapor phase is flowing out of the domain, the density of the vapor phase inside

the domain begins to reduce. However, the cohesive interaction strength controlling the liquid-vapor density ratio is not changed. Thus, for the system to come back to equilibrium, some of the high density liquid phase evaporates and brings the vapor density back to its equilibrium value. This process can continue as long as there is sufficient high density liquid phase left to evaporate. Because the cohesive interaction parameter G is related to the temperature of the system, and G is not changed, the evaporation process is isothermal and the density ratio between the liquid and vapor remains constant throughout the evaporation process. Note that condensation can be modeled by prescribing an inflow of vapor at the top of the domain.

While we have used the multiphase model of Shan and Chen [55], the evaporation mechanism can be easily incorporated into other LBM multiphase models, because it is basically driven by a reduction in the vapor pressure above the liquid phase. Although this mechanism cannot incorporate nonisothermal effects like latent heat transfer at the liquid-vapor interface, the evaporation process used here is very simple to implement and does not lead to stability problems as long as the outflow velocity u_z is small compared to the speed of sound in the system ($c_s=1/\sqrt{3}$). The evaporation mechanism used here is also more physically meaningful compared to that used in some previous LBM studies [78]. However, a limitation of the present evaporation process is that one cannot prescribe an evaporation rate directly at the liquid-vapor interface because the location of interface is not fixed and evolves as part of the solution. Whether or not it is possible to vary the evaporation rate along the liquid-vapor interface by suitably modifying the vapor outflow boundary conditions is an interesting area for further research.

III. RESULTS AND DISCUSSION

As is typically the case in LBM simulations, results are presented in lattice units, but the relevant dimensionless numbers provide the means by which results can be compared to experiments. Dimensionless numbers relevant to drop impact and spreading are discussed in the review by Yarin [79] and those typically encountered while studying the rheology of dense suspensions can be found in the review by Stickel and Powell [80]. When evaporation is present, an additional time scale related to the evaporation rate needs to be introduced. In this work, we do not consider drop impact. Thus, the velocity scale U is based on the motion of the contact line, which is driven by capillary forces. The Capillary number $Ca=U\mu/\sigma$, where μ is the dynamic viscosity and σ is the interface tension. Typical values of Ca in our simulations ranged from 0.05 to 0.10, indicating that the interface tension is the dominant force or driving mechanism. The Reynolds number $Re=UD/\nu$ based on the initial liquid drop diameter D ranged from 1 to 10, indicating that viscous forces are more dominant compared to inertial forces. The density ratio between liquid and vapor ρ_l/ρ_v is approximately 10 and that between the solid density (of suspended particles) and the surrounding liquid phase ρ_s/ρ_l is between 1.5 and 2.

When evaporation is present, the ratio of evaporation time (time for the liquid phase to reduce to a minimum value) to

spreading time for a drop (time taken to reach a maximum contact line radius) is approximately 4. In actual experiments within our group [30], the spreading time is approximately 100 to 400 ms, and the evaporation time is about 1 s, leading to a ratio of about 5 to 10. Because the intended application is studying drops whose size is around 50 to 100 μm at the most, the effects of gravity on the drop dynamics are very small and gravity is ignored completely in our simulations. This leads to a Bond number $\text{Bo}=0$ in the simulations, which is close to the experimental value of $\text{Bo}\approx 0$. Finally, the ratio of the initial liquid drop diameter to the diameter of suspended particles is approximately 10 in the present simulations but can be much larger in experiments (about 50 to 100). Because of the inherent limitations in parameter space that can be explored via LBM simulations, and because of computational limitations related to the maximum lattice size we could use, we do not expect all dimensionless parameters in this study to correspond exactly with experiments. However, an attempt has been made to approximate the flow regime in experiments to the extent possible.

A. Spreading of a pure liquid drop on a homogeneous substrate without evaporation

As one of the first examples of the present model, we examine the spreading behavior of an initially spherical liquid drop that is in contact with a fixed and homogeneous solid substrate. We first consider a case without suspended particles and validate the LBM model by comparing our predictions with the experimental results of Zosel [3]. A $201 \times 201 \times 101$ lattice was used for all these simulations, with the liquid-vapor density ratio of 10 ($g_f = -0.27$) and an equilibrium contact angles of 53° ($g_w = -0.025$). The liquid and vapor densities were $\rho_l = 1.81$ and $\rho_v = 0.18$ respectively. As mentioned before, gravity is neglected in this and in all subsequent simulations. The initial radius R_0 of the liquid drop was 43 units and the drop was initialized such that it was located at the center of the domain (along x and y) and just touched the substrate at time $t=0$.

To quantify these results, the contact line radius was scaled by the initial radius of the liquid drop R_0 and the nondimensional radius $R^* [= R(t)/R_0]$ was plotted against a nondimensional time t^* defined using $t^* = \sigma t / \mu_L^{eff} R_0$, where σ is the interface tension and μ_L^{eff} is the effective dynamic viscosity of the liquid phase. The interface tension can be obtained using Laplace's law, as discussed in Joshi and Sun [67] and for this particular case, $\sigma = 0.0548$ and for the pure liquid case, $\mu_L = \mu_L^{eff} = 0.30$. Figure 3 shows the LBM results for drop spreading for a pure liquid drop (no particles) with $\theta_{eq} = 53^\circ$ and compares the transient evolution of the contact line radius with the experimental results of Zosel [3]. The inset in Fig. 3 shows the initial and final shapes of the liquid phase assuming that the volume is unchanged during the spreading. If the final equilibrium shape is a spherical cap with an equilibrium contact angle θ_{eq} , the final contact line radius can be calculated by equating the drop volumes and this leads to

$$R_{eq}^* = \left[\frac{8}{3A + A^3} \right]^{1/3}, \quad (7)$$

where $A = [1 - \cos(\theta_{eq})] / \sin(\theta_{eq})$. For $\theta_{eq} = 53^\circ$, it can be shown using Eq. (7) that $R^* = 1.7$. It can be observed that the

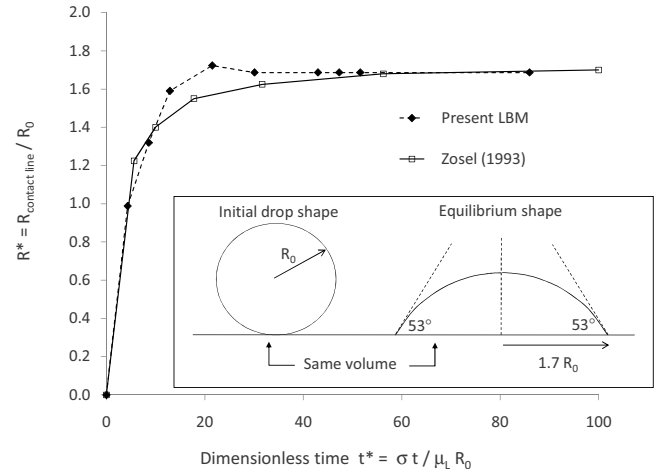


FIG. 3. Spreading dynamics for a pure liquid drop. Comparison of the LBM predictions with the experimental results of Zosel (1993) [3].

LBM results follow the same trend as the experiments, but the transient behavior is not exactly similar. In particular, it can be observed from Fig. 3 that the contact line radius in the LBM slightly overshoots the equilibrium value meaning that the drop is slightly more flattened at this point compared to experiments. One of the reasons for this discrepancy could be the relatively small density ratio (10) between the liquid and vapor phase in the LBM model. Another reason is the inability of the LBM adhesive force model (see Joshi and Sun [67] for details) to accurately simulate dynamic contact angles.

Examination of the dynamic contact angle in the LBM simulations revealed that it remains close to θ_{eq} throughout the spreading process, which is not consistent with experimental observations [3]. A similar LBM study of drop spreading [61] used the free-energy multiphase model, but the authors did not compare the dynamic contact angle predicted by their LBM model with experimental results. Sikalo *et al.* [81] suggested that the contact angle in numerical simulations be changed “*in situ*” by using empirical correlations that relate the (dynamic) contact angle to the Capillary number (based on the measured contact line velocity). In the LBM, this can be accomplished by changing the adhesive force parameter (g_w) with time instead of keeping it fixed at a value corresponding to the equilibrium contact angle. It has been recently demonstrated [7] that such an approach leads to reasonably good agreement with experiments and work is currently in progress to incorporate this approach into our model.

B. Spreading of a drop with suspended particles on a homogeneous substrate without evaporation

We now examine the spreading dynamics as a function of the suspended particle volume fraction ϕ , starting from $\phi = 0$ (no particles) and increasing to $\phi = 0.15$ (131 particles) and $\phi = 0.30$ (262 particles). A $201 \times 201 \times 101$ lattice was used for this simulation, with the liquid-vapor density ratio of 10 ($g_f = -0.27$) and an equilibrium contact angle $\theta_{eq} = 30^\circ$

($g_w = -0.037$). The liquid and vapor densities were $\rho_l = 1.81$ and $\rho_v = 0.18$, respectively, while the particle density was $\rho_{par} = 3$. The adhesive forces between the particle surface and the fluid was identical to the adhesive force between the fluid and the fixed substrate, leading to a particle contact angle $\theta_{eq,par} = 30^\circ$. This means that particles trapped in the liquid-vapor interface attain an equilibrium position such that the liquid phase forms a local contact angle of 30° with the particle surface. The initial radius R_0 of the liquid drop was 43 units and the drop was initialized such that it was located at the center of the domain (along x and y) and just touched the substrate at time $t=0$. The suspended particles were distributed randomly inside the liquid phase such that no two particles overlapped. The radius of each particle was 4.5 units. For all these simulations, the initial velocity of the liquid phase, vapor phase and of the suspended particles was zero. The same lattice size, parameter values and initial conditions were used in all subsequent simulations unless indicated otherwise.

When suspended particles are present, the effective viscosity for $\phi = 0.15$ is calculated using the Einstein correlation [82] and the effective viscosity for $\phi = 0.30$ is calculated using the Krieger-Dougherty correlation [83], which are given by Eq. (8) and Eq. (9), respectively.

$$\mu_L^{eff} = \mu_0(1 + 2.5\phi), \quad (8)$$

$$\mu_L^{eff} = \mu_0 \left(1 - \frac{\phi}{\phi_m}\right)^{-2.5\phi_m}. \quad (9)$$

In Eq. (9), ϕ_m is the maximum possible volume fraction corresponding to a close-packed structure. For a random packing of equal sized spheres, $\phi_m = 0.63$ [84].

Figure 4(a) shows the wetting behavior of a liquid drop without suspended particles. Because of adhesive forces between the liquid phase and the solid substrate, the drop begins to spread onto the substrate, eventually attaining an equilibrium contact angle $\theta_{eq} = 30^\circ$, although this final stage is not shown in Fig. 4(a). When suspended particles are added inside the liquid phase, the effective viscosity of the suspension increases. A previous numerical study [73] using a LBM suspension model has confirmed the apparent increase in viscosity and non-Newtonian (shear thickening) behavior of suspensions for single-phase flows. From Figs. 4(b) and 4(c), it can be observed that the spreading is slower when the particle volume fraction increases, confirming that a similar effect is produced even for two-phase flow considered here. Slower spreading dynamics in the presence of suspended particles because of an increase in the effective viscosity has also been documented in experiments with colloidal drops [12], providing a qualitative validation of our model results. Finally, some particle agglomeration also takes place in our simulations and particles can get trapped in the liquid-vapor interface because it is a region of local energy minimum [67].

The variation of the normalized contact line radius R^* with time for the three different particle volume fractions is summarized in Fig. 4(d). It can be seen that when the effective viscosity is used in calculating t^* , the curves for different

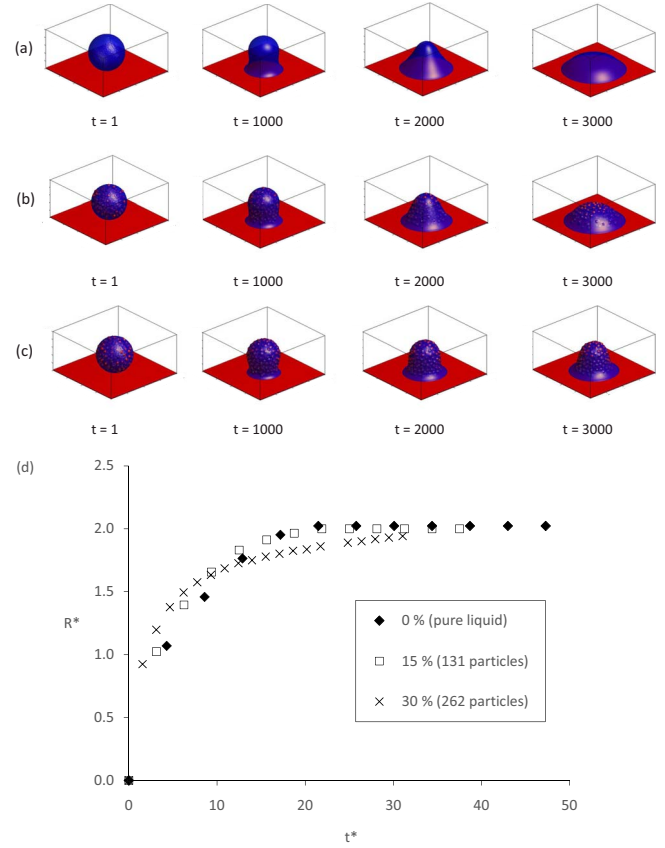


FIG. 4. (Color online) Effect of particle volume fraction on spreading dynamics for (a) pure liquid drop, (b) 15% particle volume fraction (131 particles) and (c) 30% particle volume fraction (262 particles) and (d) spreading dynamics for 0%, 15%, and 30% volume fractions in terms of the nondimensional contact line radius R^* and nondimensional time t^* .

volume fractions do not quite collapse into one master curve. One of the reasons for this might be that the particle distribution in the spreading drop does not remain uniform, leading to different effective viscosities at different locations within the drop. Thus, the effective viscosity relationships might not be strictly applicable. Whether or not one can define a single viscosity for such cases is debatable and warrants further study.

Another reason for the discrepancy is that the irreversible migration of suspended particles to the liquid-vapor interface might affect the interface tension and thus influence the spreading dynamics, which is dominated by capillary forces. This aspect has been investigated by a few experimental studies on colloidal dispersions. Dong and Johnson [85,86] concluded that for low concentrations of particles (up to 5% by weight), the interface tension decreased markedly. However, when the suspended particles were more than approximately 15% by weight, the interface tension of a colloidal drop was only slightly higher the interface tension of a pure liquid drop with no suspended particles. In addition, the interface tension was independent of the particle concentration if none of the particles were on the interface [86]. Another study by Vignati and Piazza [87] found that the interface tension for an oil-water emulsion was not significantly

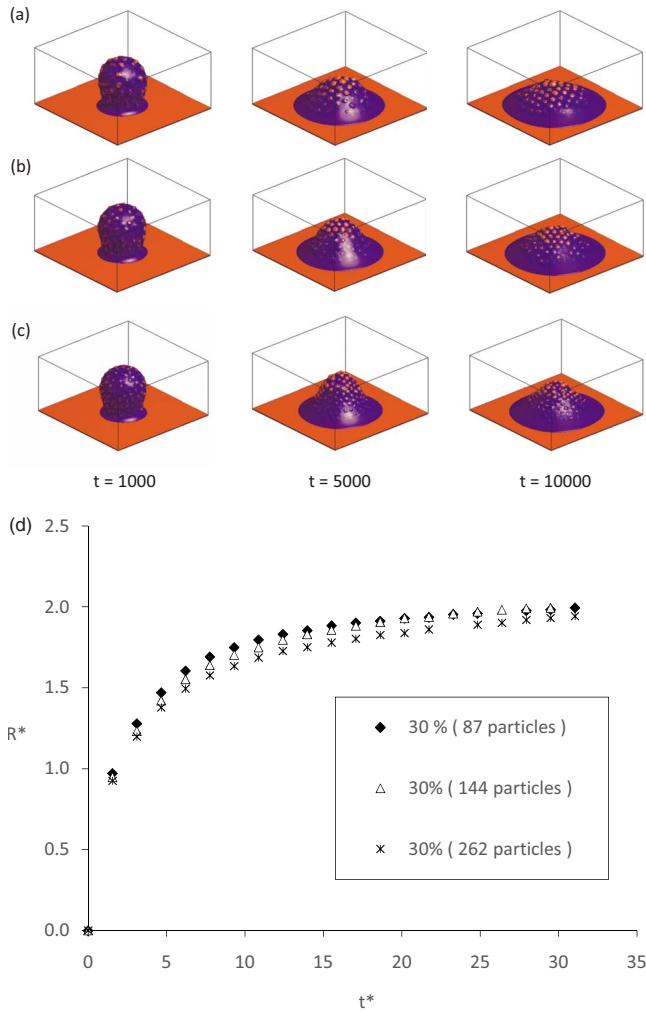


FIG. 5. (Color online) Spreading dynamics for different particle sizes for a particle volume fraction of 30% (a) 87 particles, (b) 144 particles, (c) 262 particles, and (d) evolution of contact line radius for different particle sizes in terms of the nondimensional contact line radius R^* and nondimensional time t^* .

changed by the presence and concentration of silica particles. A recent review by Hunter *et al.* [88] does find evidence of the interface tension being affected by suspended particles and the particle size, wetting properties and surface roughness all seem to play a role. For colloidal drop spreading, isolating the effects of changes in effective viscosity and changes in interfacial tension due to suspended particles is an interesting area for further research and the present model will be useful to carry out a detailed investigation.

To examine whether the spreading dynamics is sensitive to the size of the suspended particles relative to the size of the liquid drop, we carried out LBM simulations for a fixed particle volume fraction of 30% but for a smaller number of particles compared to those in Fig. 4(c). The particle radius for each case was adjusted such that the combined volume of all particles remains constant. For the case of 144 particles, the particle radius was 5.495 and for the case of 87 particles, the particle radius used was 6.5. The results are summarized in Figs. 5(a)–5(c), where the drop morphology is shown at different times during spreading. It can be observed that the

particles are clustered near the center of the liquid drop and the volume near the contact line is relatively free of suspended particles. The reason for this particle clustering is not yet clear, but apparently depends on the adhesive force between the particle surface and the surrounding liquid phase. We find that a suspension of hydrophilic particles show stronger clustering compared to an otherwise similar suspension of hydrophobic particles. In general, suspended particles in the LBM model do not behave like passive tracers during drop spreading and have a strong influence on the wetting dynamics. These cases will be reexamined in greater detail after adding in DLVO forces in our model. The nondimensional contact line radius R^* for these cases is shown in Fig. 5(d). It can be observed that as the number of particles increases, the spreading is slightly slower. However, this slowdown effect is not very significant, indicating that the size of the suspended particles relative to the drop size has a relatively small effect on the spreading dynamics for a fixed volume fraction. Our prediction that the spreading dynamics for a given volume fraction is independent of the particle size is also consistent with experiments [12], providing additional validation of our model.

C. Spreading of a drop containing suspended particles on patterned substrates without evaporation

If the substrate is patterned into a series of bands with different surface energies, drop spreading takes place in a preferential manner such that it is repelled from the lower surface energy areas of the substrate and attracted toward the high surface energy areas. This enables more accurate positioning of the drop (and the eventual deposition of particles during inkjet printed electronics) if the initial impact point is hard to control precisely. In order to demonstrate this idea, we consider a nonevaporating colloidal drop containing 90 suspended particles (10% by volume), which is initially spherical and contacts the substrate at the boundary between the patterned areas. A $250 \times 250 \times 100$ lattice was used for this simulation. The central band in the pattern is hydrophilic and 70 lattice units in width and the side bands are relatively hydrophobic. Figure 6 shows how the initially offset drop containing suspended particles is gradually and automatically moved into the central hydrophilic band (corresponding to a $\theta_{eq} = 30^\circ$) and repelled from the relatively low energy side bands. In the absence of contact line pinning, the drop moves into the central hydrophilic band irrespective of the initial offset or of the relative thicknesses of the bands. This was confirmed via LBM simulations for different wetting parameters (equilibrium contact angles) and for different relative widths of the bands.

However, the rate at which the drop moves into the hydrophilic band is affected both by the effective viscosity of the drop and by the relative wetting strengths of the bands. In Figs. 6(a)–6(c), the (central) hydrophilic band has an equilibrium contact angle of 30° , but the side bands have equilibrium contact angles of 60° , 90° , and 120° , respectively. It can be seen that the drop movement is much faster in Figs. 6(b) and 6(c) because of the reducing surface energy in the side bands. To quantify this effect, we have normalized the

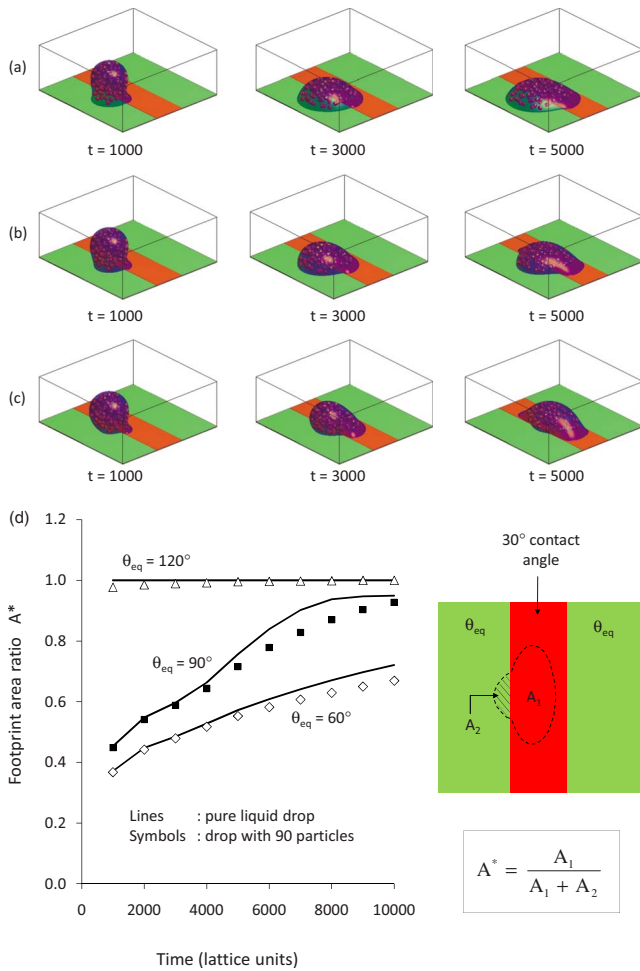


FIG. 6. (Color online) Effect of surface wetting strength on drop dynamics for a liquid drop containing 90 particles (10% volume fraction) with an initial offset such that the drop impacts the substrate outside the central band. The equilibrium contact angles for the side bands are (a) 60° , (b) 90° , and (c) 120° . The equilibrium contact angle in the central (hydrophilic) band is 30° for all cases. (d) Fraction of drop footprint in the central band for various surface energies for a pure liquid drop and a colloidal drop with 90 particles.

area (footprint) of the spreading drop in the central band with the entire footprint of the drop and plotted this ratio as a function of spreading time. This plot is shown in Fig. 6(d). When $A^*=1$, the entire drop is in the central band. For the cases where the side bands have contact angles of 60° and 90° , it can be seen that A^* approaches unity gradually, but for the case of hydrophobic side bands ($\theta_{eq}=120^\circ$), the movement of the base of the drop to the central portion of the substrate appears almost instantaneous because the initial transient (below $t=1000$) was not recorded.

Keeping all other parameters identical, each of these three cases was also run for a pure liquid drop without any suspended particles and these results are indicated in Fig. 6(d) by solid lines. It can be observed that the drop without particles moves into the central band more rapidly compared to the colloidal drop. This observation can be explained on the basis of an increase in viscosity for the colloidal drop, which tends to reduce the rate at which it moves into the central

band. The speed at which droplets move can be an important factor in controlling the deposition of suspended particles in the presence of evaporation. For example, if the evaporation rate is very high, a slow-moving drop may not finish moving into the desired area of the substrate and final deposition will not be accurate.

D. Evaporation of a pure liquid drop on a homogeneous substrate

Before simulating the evaporation of drops with suspended particles, it is useful to examine in detail the evaporation of a hemispherical liquid drop located on a homogeneous substrate and containing no suspended particles. We will first discuss our results and then compare them with evaporation mechanisms found in experiments and in some previous numerical simulations. The LBM simulations were carried out using a $201 \times 201 \times 101$ lattice. The equilibrium contact angle of the liquid drop was set to 90° ($g_w=0$) and the initial shape of the liquid phase was a hemispherical cap of radius 73 lattice units. The drop was placed on a fixed, homogeneous substrate ($z=1$) and was located such that the center of the drop was at $(100,100,1)$. The vapor velocity at the top face was set at $u_z=0.01$.

Figure 7(a) shows the schematic of the problem and the cross-sectional view of the liquid-vapor interface at $t=3000$, $t=6000$, $t=9000$, $t=12000$, $t=15000$, and $t=18000$. It can be observed that: 1. The evaporation rate is uniform all along the interface, 2. The radius of the drop reduces slowly at first and rapidly at later times and 3. The contact angle remains unchanged throughout the evaporation process. To quantify these observations, the volume of the liquid drop was calculated at various times and this plot is shown in Fig. 7(b). It can be clearly seen that the volume reduces linearly with time, indicating that the rate of change of volume with time is constant and independent of the drop radius. This result is expected because the rate at which mass is being removed from the system at the top boundary is constant. Note that a similar result can be obtained using a moving piston boundary condition at the top, like the one used by Lee and Lin [89]. In both the present evaporation model and the model used in Ref. [89], the evaporation process is driven by a change in the vapor pressure above the liquid phase.

The evaporation of a liquid drop on a substrate has been the focus of many experimental studies [17,22,24,90,91]. Most of these experiments deal with the evaporation of a liquid drop in air and the evaporation process at the liquid-air interface is driven by concentration gradients of the liquid at the interface and in the surrounding air. For example, the rate of evaporation of water drops is a function of the relative humidity of the surrounding air. The evaporation process itself is found to occur in distinct stages, depending on the surface roughness. For drops evaporating on smooth substrates, the drop contact area and drop height both reduce with time, leading to a self-similar shrinkage with a constant contact angle. For rough substrates, the drop contact area remains constant in the initial stage of evaporation but the drop height reduces. Thus, the contact angle keeps reducing. This continues until the (receding) contact angle falls below

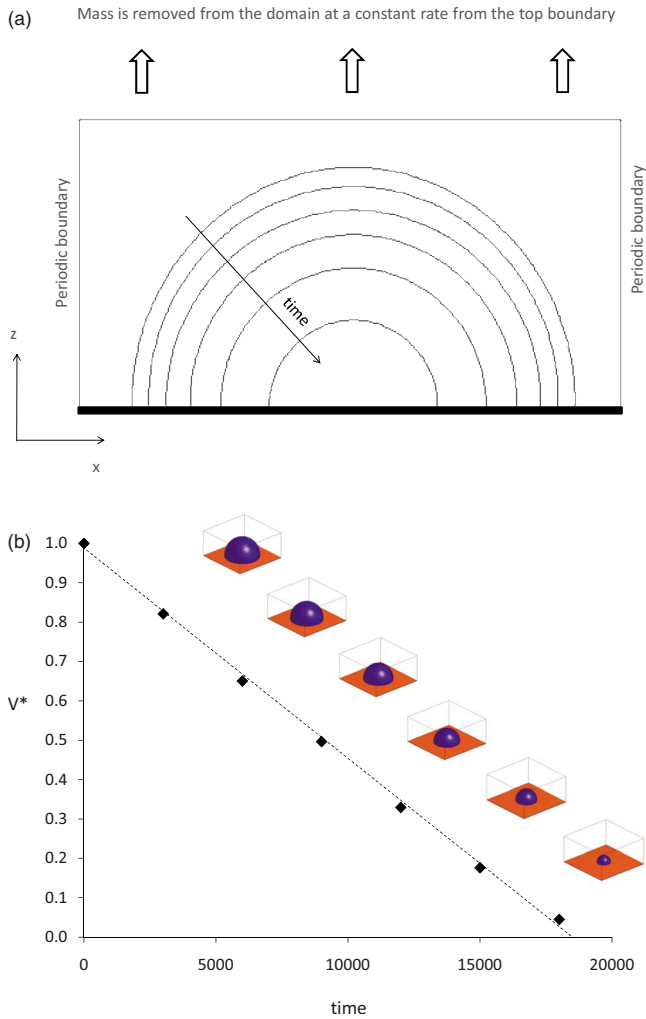


FIG. 7. (Color online) (a) Cross-sectional views of the liquid-vapor interface for an evaporating hemispherical drop (equilibrium contact angle 90°). The evaporation rate is uniform along the liquid-vapor interface and the drop shrinks faster at later times because the interface area decreases. The contact angle remains unchanged. (b) Normalized volume of an evaporating liquid drop. The symbols represent LBM data points and the dashed line is a linear fit to the data points.

a critical value. Beyond this point, the contact area starts reducing and the contact angle remains roughly constant. Finally, in the last stage, both the contact area and the contact angle reduce.

At present, the LBM model is only able to simulate the second evaporation stage, where the contact angle remains constant and the contact line shrinks. Also, in contrast to most experiments, the present LBM simulations model a single component, two-phase system, like pure water surrounded by water-vapor and mass diffusion is not considered. For pure liquid drops evaporating on a atomically smooth substrate like freshly cleaved mica, the evaporation process observed in experiments is similar to that observed in the present LBM, in that the contact line does not pin [17,22]. However, this is not generally true even for pure liquids evaporating on a substrate. Measurements on evaporating water drops have shown that a linear reduction of liq-

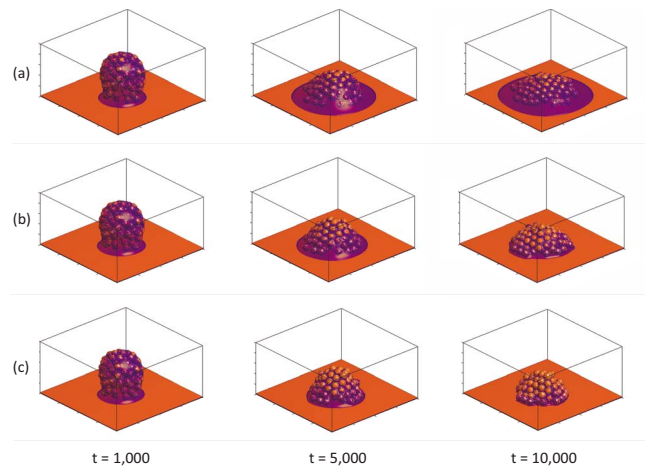


FIG. 8. (Color online) Effect of evaporation on the drop dynamics and particle deposition for a liquid drop containing 87 particles (30% initial volume fraction). The equilibrium contact angle is 30° (a) The case without evaporation, (b) evaporation induced by prescribing a vapor outflow velocity ($u_z=0.005$) at the top boundary, (c) evaporation induced by prescribing a vapor outflow velocity ($u_z=0.01$) at the top boundary.

uid drop volume with time (constant evaporation rate), as shown in Fig. 7(b), typically corresponds to the case of pinned evaporation [90]. The evaporation rate peaks at the contact line and is therefore proportional to the contact line perimeter. Nonisothermal evaporation models and thermal effects like Marangoni flow are beyond the scope of the present study, but contact line pinning can be simulated in our model by using locally varying surface energies. This aspect will be explored more fully in our future work and is not discussed further here.

E. Drop spreading, evaporation and particle deposition on a homogeneous substrate

We now examine the spreading behavior of a suspension in the presence of evaporation. In Fig. 8(a), a case without evaporation is shown for a particle volume fraction of 30% and with 87 particles. As observed before, the contact line radius increases until the equilibrium contact angle (30° in this case) is attained. In Fig. 8(b), the same case is repeated with a velocity of $u_z=0.005$ imposed for the vapor phase at the top boundary. It can be observed that the spreading dynamics at $t=5000$ and $t=10000$ are substantially different compared to Fig. 8(a). As a consequence of liquid evaporation, the suspended particles are confined to a smaller and smaller volume, eventually resulting in a random close-packed arrangement of the particles inside the liquid phase. A simulation with an even higher evaporation rate, corresponding to $u_z=0.01$ is depicted in Fig. 8(c), where the particles are seen to be packed more closely compared to Fig. 8(b).

The volume of the liquid phase in the suspension was examined as a function of time for $u_z=0.005$ and $u_z=0.01$ and the results are summarized in Fig. 9. It can be observed from Fig. 9 that a faster evaporation rate leads to a more

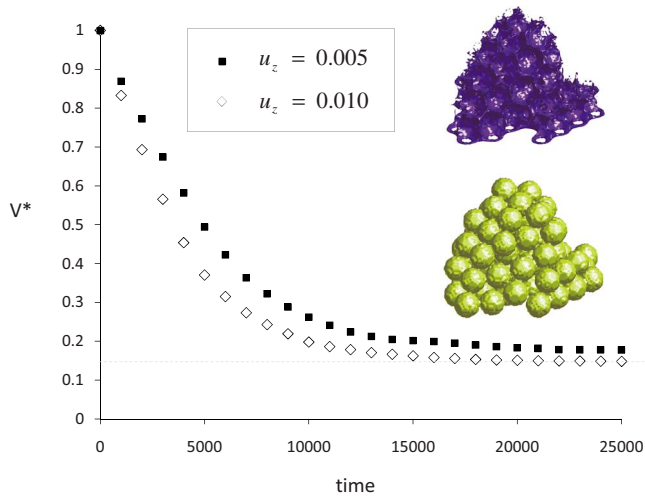


FIG. 9. (Color online) Evolution of the liquid volume with time for an evaporating suspension for two different evaporation rates. The liquid volume is normalized using the initial liquid volume. The insets show the arrangement of suspended particles on the substrate and the morphology of liquid phase in the interstitial spaces between particles after the suspension has been evaporating ($u_z = 0.01$) for 20 000 time steps.

rapid depletion of the liquid phase. However, beyond a certain point, the liquid phase no longer evaporates and about 15% of the original liquid remains in the system even after a long time. This result should be contrasted with that obtained for a pure liquid [Fig. 7(b)], where all the liquid phase eventually evaporates. The insets in Fig. 9 show the suspended particle assembly and the liquid phase at $t=20\,000$ and one can observe that the particles are closely packed, and liquid occupies the interstitial spaces between particles. The inability of all the liquid phase to evaporate is because of capillary pressure of the wetting liquid (local $\theta_{eq} = 30^\circ$) in between narrow interstitial spaces, which creates a lower pressure in the liquid compared to the vapor. It was confirmed that using a larger suction velocity ($u_z = 0.02$) at the top of the domain reduces this residual liquid phase. In addition, the final residual liquid may also become disconnected and form discrete liquid bridges between neighboring solid particles.

Turner *et al.* [92] carried out an experimental investigation to find out the *irreducible water saturation* in a porous medium composed of monodisperse acrylic beads using vegetable oil as the liquid phase. The liquid volume fraction left behind after draining the porous medium overnight was measured to be 13%, which is similar to the LBM prediction for the residual liquid volume. In addition, the morphology of the liquid phase trapped in the pore space between the closely packed beads, observed using microcomputed tomography (μ CT), is very similar to that predicted by the LBM [Fig. 9 (inset)]. As discussed in Ref. [92], the trapped wetting phase can exist as pendular rings between grains, as liquid bridges separated by a small gap, or as complicated structures formed by a combination of these individual morphologies. The experimental results of Ref. [92] thus provide a good validation of the LBM predictions and our model can be a useful tool for simulating the drying of porous materials.

Because there is no gravity in these simulations and mainly because of capillary interactions, the particles can

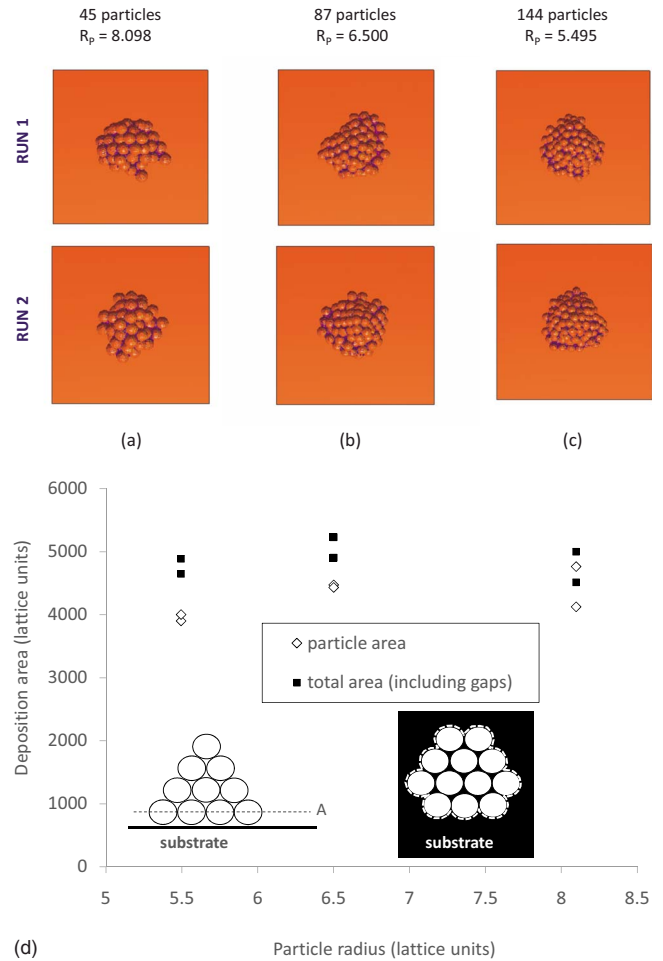


FIG. 10. (Color online) Effect of particle size on final particle deposition area for an initial particle volume fraction of 30%, equilibrium contact angle of 30° and a vapor outflow velocity ($u_z = 0.01$) at the top boundary. (a) 45 particles of radius 8.1, (b) 87 particles of radius 6.5, and (c) 144 particles of radius 5.5. (d) Measurement of the deposit area for various particle sizes. The inset on the left shows the side view of the final deposit heap with the dashed line representing plane “A” where area measurements are performed. The top view shows the cross section of particles in plane “A” and gaps in between particles.

form closely packed structures without collapsing on the substrate. This type of particle assembly can be used for example to build photonic crystals [93] or for depositing electrically conducting material on flexible substrates using inkjet printing. It may also help model the stability of granular materials like wet sand, where capillary forces between sand particles can be strong enough to build noncollapsible structures like sand castles. Note that even if the equilibrium contact angle of the carrier liquid phase with the substrate is 30° , the particles do not spread out to this value because evaporation rate is very fast and most of the liquid phase evaporates before it has had a chance to spread completely.

Motivated by the experimental results in Ref. [23], we examined the effect of using different particle sizes on the final deposition of particles. Figures 10(a)–10(c) shows the final particle deposit for three different particle sizes in top view. Because the final deposit also depends on the initially

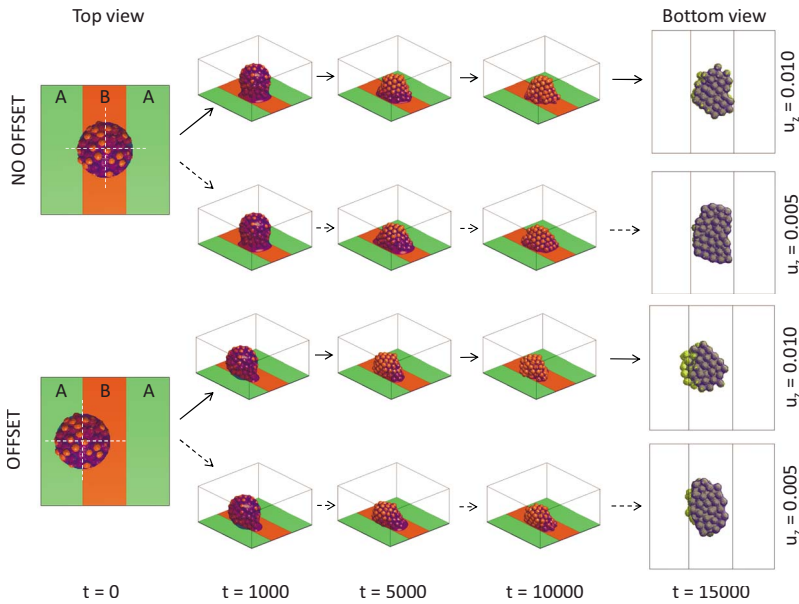


FIG. 11. (Color online) Effect of evaporation rate and initial offset on the drop dynamics and particle deposition for a liquid drop containing 87 particles (30% initial volume fraction) and spreading on a patterned substrate (equilibrium contact angles: $A=150^\circ$, $B=30^\circ$). The top views show the impact location relative to the substrate and the bottom views show the final particle deposition on the substrate.

random placement of particles inside the liquid drop, each run leads to a slightly different deposition pattern. We illustrate this effect for two runs in Fig. 10. It can be observed that the final deposit area remains approximately constant for the range of particle sizes considered here. In order to quantify these results, the cross-sectional area of the particles closest to the substrate was measured in a plane (indicated by “A”) that cut through the equators of the particles as shown in the inset in Fig. 10(d). Two sets of measurements were taken. In the first set of measurements, the gap in between the packed particles was excluded, while in the second, the deposit area corresponded to the envelope indicated by the white dashed line [inset, Fig. 10(d)]. The scatter in the data for a given particle size is because of the different initial arrangement, but overall the deposition area is almost constant. This is in contrast to the findings of Ref. [23], who observe a smaller deposit footprint when particle size is smaller. This discrepancy might be because deposits from larger particles do not form close-packed structures in the experiments, leading to significant empty space in between particles [23]. In the present LBM simulations, the final deposits are approximately close-packed and also of a similar shape. Note that these comparisons are only qualitative because the experimental suspensions were colloidal (particle size ranged from 0.3 to 3 micron), very dilute (1 wt %) and the substrates used were hydrophobic ($\theta_{eq}=103^\circ$).

F. Drop spreading, evaporation, and particle deposition on a patterned substrate

If the substrate is patterned into hydrophobic and hydrophilic bands, the deposition dynamics is affected by two parallel processes. The first of these is the spreading or wetting behavior and the second is the rate of evaporation. In Fig. 11 (top two rows), results for a drop that impacts exactly at the center of the hydrophilic band is shown. The substrate pattern is such that the equilibrium contact angles are 30° and 150° in the hydrophilic (B) and hydrophobic (A) bands, respectively. When $u_z=0.01$, the carrier liquid evaporates very

rapidly and the drop does not have time to wet the central band completely. Thus, the final particle deposit shows an effective contact angle much larger than 30° and only a slight spreading in the hydrophilic band is observed. When the evaporation rate is reduced ($u_z=0.005$), the liquid gets some more time to spread before it evaporates. Consequently, the final deposit shows a distinct elongation along the hydrophilic band.

It can be observed that all the particles eventually form a close-packed structure and get deposited on the hydrophilic band. The bottom two rows in Fig. 11 show the results for cases when the initial drop position is offset such that it impacts the substrate at a point which is exactly midway between the two bands. Again, the competing effects of drop spreading and evaporation can be observed from the final deposition, which is more elongated if the evaporation rate is lower. It can be observed that even for these two cases, the final particle deposition takes place in the central (hydrophilic) band. Thus, the effect of the initial offset in the drop impact point on the final particle deposition can be substantially reduced by controlling the surface energies of the substrate.

IV. CONCLUSIONS

In this work, we have shown that the lattice Boltzmann method (LBM) can be a useful tool for simulating the dynamics of colloidal drops as they spread and evaporate on homogeneous and patterned substrates. An important effect of the suspended particles is increasing the apparent viscosity of the drop compared to the pure liquid phase. Aggregation of particles due to interparticle forces and trapping of particles in the liquid-vapor interface are other effects that can have an impact on the spreading dynamics and/or the final deposition of the particles once the carrier liquid evaporates. Qualitative agreement was reached with prior experimental work [12] regarding the effect of particle concentration (higher concentration slows down the spreading) and

particle size (no significant effect) on the spreading dynamics.

Evaporation has been modeled by sucking out vapor from the domain, thereby reducing the vapor pressure above the liquid drop. The liquid drop consequently evaporates to replenish the lost vapor and the liquid-vapor density ratio in the system does not change. The evaporation process is isothermal and corresponds to the constant contact angle evaporation mode observed in experiments. For a pure liquid drop on a smooth and homogeneous substrate, evaporation leads to a uniform reduction of drop volume with time until all the liquid phase evaporates. For drops with suspended particles evaporating on a substrate, evaporation leads to the suspended particles being packed closely together and a finite amount of liquid phase remains trapped in the gaps between particles. This trapped liquid does not evaporate unless its capillary pressure can be overcome and may form discrete liquid bridges, pendular rings and other complex morphologies between particle pairs. Qualitative agreement was obtained with respect to the amount of residual liquid and the liquid phase morphology between the present LBM predictions and the experimental studies of drainage in a porous medium [92]. The final particle deposition can be controlled by the evaporation rate and by the surface energy of the substrate. Using patterned substrates can help achieve particle deposition at desired locations even when the initial impact point of the suspension is not controllable.

A limitation of the current LBM approach is the inability to model nonisothermal flows and latent heat transfer during the phase change process. Future work in this area can focus on the role of interparticle DLVO forces, Brownian motion, effect of particle surface energy (hydrophobic/hydrophilic/neutral wetting) and concentration on the interface tension, heat transfer related effects like Marangoni flow and further validation of the model with experiments. Apart from colloidal drop dynamics, some of the additional applications of this model include studying the drying of porous media, modeling wet granular materials (like wet sand) and in investigating the impact of evaporation/condensation processes during the two-phase transport of water and water-vapor in porous polymer electrolyte membrane (PEM) fuel cell electrodes.

ACKNOWLEDGMENTS

The authors would like to thank the National Science Foundation (Grant No. CAREER-0968927) and American Chemical Society Petroleum Research Fund (Grant No. 47731-G9) for providing financial support. We also thank Viral Chhasatia, Shun Su and Anita Gokhlay for their help in running some of the simulations and analyzing the results.

APPENDIX A: 3D IMPLICIT SCHEME FOR UPDATING LINEAR AND ANGULAR VELOCITY OF A SINGLE SUSPENDED PARTICLE

In this appendix, we extend the implicit particle velocity update scheme [53], adapted in our previous work to a 2D multiphase particle suspension model [67], to 3D and include

interparticle forces within the framework. The basic idea is that the (unknown) linear and angular particle velocities at the new time level are to be used while calculating the velocity of node points at the boundary of suspended particles. This *boundary node velocity* includes both translational and rotational components of the particle velocity and is given by

$$\mathbf{u}_b = \mathbf{U} + \boldsymbol{\Omega} \times (\mathbf{r}_b - \mathbf{R}), \quad (\text{A1})$$

where \mathbf{U} is the translational velocity of the particle, $\boldsymbol{\Omega}$ is the angular velocity, \mathbf{r}_b is the location of the boundary node and \mathbf{R} is the location of the center of mass of the particle.

Expressions for the forces and torques acting on the particle of mass M and moment of inertia I are first derived using the three (unknown) linear velocity components at the new time level (u_x, u_y, u_z) and the three (unknown) angular velocities of the particle at the new time level ($\Omega_x, \Omega_y, \Omega_z$). Newton's second law is then applied to relate forces (along x , y , and z) and torques (along x , y , and z) to the change in the linear and angular velocities of the particle. The result is a set of six linear equations that can be solved for the six unknowns ($u_x, u_y, u_z, \Omega_x, \Omega_y, \Omega_z$). After some algebra, the resulting system of equations can be written as

$$\begin{pmatrix} A_{11} & A_{12} & A_{13} & A_{14} & A_{15} & A_{16} \\ A_{21} & A_{22} & A_{23} & A_{24} & A_{25} & A_{26} \\ A_{31} & A_{32} & A_{33} & A_{34} & A_{35} & A_{36} \\ A_{41} & A_{42} & A_{43} & A_{44} & A_{45} & A_{46} \\ A_{51} & A_{52} & A_{53} & A_{54} & A_{55} & A_{56} \\ A_{61} & A_{62} & A_{63} & A_{64} & A_{65} & A_{66} \end{pmatrix} \begin{pmatrix} u_x \\ u_y \\ u_z \\ \Omega_x \\ \Omega_y \\ \Omega_z \end{pmatrix} = \begin{pmatrix} B_1 \\ B_2 \\ B_3 \\ B_4 \\ B_5 \\ B_6 \end{pmatrix}. \quad (\text{A2})$$

The elements of the coefficient matrix are given by

$$A_{11} = 1 + \frac{6}{M} \sum_{bn} \sum_{\alpha} \rho w_{\alpha} \mathbf{e}_{\alpha x} \mathbf{e}_{\alpha x}, \quad (\text{A3})$$

$$A_{22} = 1 + \frac{6}{M} \sum_{bn} \sum_{\alpha} \rho w_{\alpha} \mathbf{e}_{\alpha y} \mathbf{e}_{\alpha y}, \quad (\text{A4})$$

$$A_{33} = 1 + \frac{6}{M} \sum_{bn} \sum_{\alpha} \rho w_{\alpha} \mathbf{e}_{\alpha z} \mathbf{e}_{\alpha z}, \quad (\text{A5})$$

$$A_{44} = 1 + \frac{6}{I} \sum_{bn} \sum_{\alpha} (\rho w_{\alpha} r_y r_y \mathbf{e}_{\alpha z} \mathbf{e}_{\alpha z} + \rho w_{\alpha} r_z r_z \mathbf{e}_{\alpha y} \mathbf{e}_{\alpha y} - 2\rho w_{\alpha} r_y r_z \mathbf{e}_{\alpha y} \mathbf{e}_{\alpha z}), \quad (\text{A6})$$

$$A_{55} = 1 + \frac{6}{I} \sum_{bn} \sum_{\alpha} (\rho w_{\alpha} r_x r_x \mathbf{e}_{\alpha z} \mathbf{e}_{\alpha z} + \rho w_{\alpha} r_z r_z \mathbf{e}_{\alpha x} \mathbf{e}_{\alpha x} - 2\rho w_{\alpha} r_x r_z \mathbf{e}_{\alpha x} \mathbf{e}_{\alpha z}), \quad (\text{A7})$$

$$A_{66} = 1 + \frac{6}{I} \sum_{bn} \sum_{\alpha} (\rho w_{\alpha} r_x r_x \mathbf{e}_{\alpha y} \mathbf{e}_{\alpha y} + \rho w_{\alpha} r_y r_y \mathbf{e}_{\alpha x} \mathbf{e}_{\alpha x} - 2\rho w_{\alpha} r_x r_y \mathbf{e}_{\alpha x} \mathbf{e}_{\alpha y}), \quad (\text{A8})$$

$$A_{12} = A_{21} = \frac{6}{M} \sum_{bn} \sum_{\alpha} \rho w_{\alpha} \mathbf{e}_{\alpha y} \mathbf{e}_{\alpha x}, \quad (\text{A9})$$

$$A_{13} = A_{31} = \frac{6}{M} \sum_{bn} \sum_{\alpha} \rho w_{\alpha} \mathbf{e}_{\alpha z} \mathbf{e}_{\alpha x}, \quad (\text{A10})$$

$$A_{23} = A_{32} = \frac{6}{M} \sum_{bn} \sum_{\alpha} \rho w_{\alpha} \mathbf{e}_{\alpha z} \mathbf{e}_{\alpha y}, \quad (\text{A11})$$

$$A_{14} = \frac{I}{M} A_{41} = -\frac{6}{M} \sum_{bn} \sum_{\alpha} (\rho w_{\alpha} r_z \mathbf{e}_{\alpha y} \mathbf{e}_{\alpha x} - \rho w_{\alpha} r_y \mathbf{e}_{\alpha z} \mathbf{e}_{\alpha x}), \quad (\text{A12})$$

$$A_{15} = \frac{I}{M} A_{51} = -\frac{6}{M} \sum_{bn} \sum_{\alpha} (\rho w_{\alpha} r_x \mathbf{e}_{\alpha z} \mathbf{e}_{\alpha x} - \rho w_{\alpha} r_z \mathbf{e}_{\alpha x} \mathbf{e}_{\alpha x}), \quad (\text{A13})$$

$$A_{16} = \frac{I}{M} A_{61} = -\frac{6}{M} \sum_{bn} \sum_{\alpha} (\rho w_{\alpha} r_y \mathbf{e}_{\alpha x} \mathbf{e}_{\alpha x} - \rho w_{\alpha} r_x \mathbf{e}_{\alpha y} \mathbf{e}_{\alpha x}), \quad (\text{A14})$$

$$A_{24} = \frac{I}{M} A_{42} = -\frac{6}{M} \sum_{bn} \sum_{\alpha} (\rho w_{\alpha} r_z \mathbf{e}_{\alpha y} \mathbf{e}_{\alpha y} - \rho w_{\alpha} r_y \mathbf{e}_{\alpha z} \mathbf{e}_{\alpha y}), \quad (\text{A15})$$

$$A_{25} = \frac{I}{M} A_{52} = -\frac{6}{M} \sum_{bn} \sum_{\alpha} (\rho w_{\alpha} r_x \mathbf{e}_{\alpha z} \mathbf{e}_{\alpha y} - \rho w_{\alpha} r_z \mathbf{e}_{\alpha x} \mathbf{e}_{\alpha y}), \quad (\text{A16})$$

$$A_{26} = \frac{I}{M} A_{62} = -\frac{6}{M} \sum_{bn} \sum_{\alpha} (\rho w_{\alpha} r_y \mathbf{e}_{\alpha x} \mathbf{e}_{\alpha y} - \rho w_{\alpha} r_x \mathbf{e}_{\alpha y} \mathbf{e}_{\alpha y}), \quad (\text{A17})$$

$$A_{34} = \frac{I}{M} A_{43} = -\frac{6}{M} \sum_{bn} \sum_{\alpha} (\rho w_{\alpha} r_z \mathbf{e}_{\alpha y} \mathbf{e}_{\alpha z} - \rho w_{\alpha} r_y \mathbf{e}_{\alpha z} \mathbf{e}_{\alpha z}), \quad (\text{A18})$$

$$A_{35} = \frac{I}{M} A_{53} = -\frac{6}{M} \sum_{bn} \sum_{\alpha} (\rho w_{\alpha} r_x \mathbf{e}_{\alpha z} \mathbf{e}_{\alpha z} - \rho w_{\alpha} r_z \mathbf{e}_{\alpha x} \mathbf{e}_{\alpha z}), \quad (\text{A19})$$

$$A_{36} = \frac{I}{M} A_{63} = -\frac{6}{M} \sum_{bn} \sum_{\alpha} (\rho w_{\alpha} r_y \mathbf{e}_{\alpha x} \mathbf{e}_{\alpha z} - \rho w_{\alpha} r_x \mathbf{e}_{\alpha y} \mathbf{e}_{\alpha z}), \quad (\text{A20})$$

$$A_{45} = A_{54} = \frac{6}{I} \sum_{bn} \sum_{\alpha} (\rho w_{\alpha} r_y r_z \mathbf{e}_{\alpha x} \mathbf{e}_{\alpha z} - \rho w_{\alpha} r_x r_y \mathbf{e}_{\alpha z} \mathbf{e}_{\alpha z} + \rho w_{\alpha} r_x r_z \mathbf{e}_{\alpha y} \mathbf{e}_{\alpha z} - \rho w_{\alpha} r_z r_x \mathbf{e}_{\alpha x} \mathbf{e}_{\alpha y}), \quad (\text{A21})$$

$$A_{46} = A_{64} = \frac{6}{I} \sum_{bn} \sum_{\alpha} (\rho w_{\alpha} r_x r_y \mathbf{e}_{\alpha y} \mathbf{e}_{\alpha z} - \rho w_{\alpha} r_y r_x \mathbf{e}_{\alpha z} \mathbf{e}_{\alpha x} + \rho w_{\alpha} r_y r_z \mathbf{e}_{\alpha x} \mathbf{e}_{\alpha y} - \rho w_{\alpha} r_z r_x \mathbf{e}_{\alpha y} \mathbf{e}_{\alpha y}), \quad (\text{A22})$$

$$A_{56} = A_{65} = \frac{6}{I} \sum_{bn} \sum_{\alpha} (\rho w_{\alpha} r_z r_x \mathbf{e}_{\alpha x} \mathbf{e}_{\alpha y} - \rho w_{\alpha} r_z r_y \mathbf{e}_{\alpha x} \mathbf{e}_{\alpha x} + \rho w_{\alpha} r_x r_y \mathbf{e}_{\alpha z} \mathbf{e}_{\alpha x} - \rho w_{\alpha} r_x r_x \mathbf{e}_{\alpha y} \mathbf{e}_{\alpha z}). \quad (\text{A23})$$

The right-hand side of Eq. (A2) is calculated using

$$B_1 = u_{x,0} + \frac{2}{M} \sum_{bn} \sum_{\alpha} f_{\alpha}^{+} \mathbf{e}_{\alpha x} + \frac{1}{M} \sum_{bn} \mathbf{F}_{adh,x}^p + \frac{1}{M} [\mathbf{F}_{U,x}^p + \mathbf{F}_{C,x}^p + \mathbf{F}_{lub,x}^p + \mathbf{F}_{Hook,x}^p], \quad (\text{A24})$$

$$B_2 = u_{y,0} + \frac{2}{M} \sum_{bn} \sum_{\alpha} f_{\alpha}^{+} \mathbf{e}_{\alpha y} + \frac{1}{M} \sum_{bn} \mathbf{F}_{adh,y}^p + \frac{1}{M} [\mathbf{F}_{U,y}^p + \mathbf{F}_{C,y}^p + \mathbf{F}_{lub,y}^p + \mathbf{F}_{Hook,y}^p], \quad (\text{A25})$$

$$B_3 = u_{z,0} + \frac{2}{M} \sum_{bn} \sum_{\alpha} f_{\alpha}^{+} \mathbf{e}_{\alpha z} + \frac{1}{M} \sum_{bn} \mathbf{F}_{adh,z}^p + \frac{1}{M} [\mathbf{F}_{U,z}^p + \mathbf{F}_{C,z}^p + \mathbf{F}_{lub,z}^p + \mathbf{F}_{Hook,z}^p], \quad (\text{A26})$$

$$B_4 = \Omega_{x,0} + \frac{2}{I} \sum_{bn} \sum_{\alpha} (r_y f_{\alpha}^{+} \mathbf{e}_{\alpha z} - r_z f_{\alpha}^{+} \mathbf{e}_{\alpha y}) + \frac{1}{I} \sum_{bn} (r_y \mathbf{F}_{adh,z}^p - r_z \mathbf{F}_{adh,y}^p) - \frac{1}{I} \sum_U (r_{U,y} \bar{\rho}_U \mathbf{u}_{U,z} - r_{U,z} \bar{\rho}_U \mathbf{u}_{U,y}) + \frac{1}{I} \sum_C (r_{C,y} \rho_C \mathbf{u}_{C,z} - r_{C,z} \rho_C \mathbf{u}_{C,y}), \quad (\text{A27})$$

$$B_5 = \Omega_{y,0} + \frac{2}{I} \sum_{bn} \sum_{\alpha} (r_z f_{\alpha}^{+} \mathbf{e}_{\alpha x} - r_x f_{\alpha}^{+} \mathbf{e}_{\alpha z}) + \frac{1}{I} \sum_{bn} (r_z \mathbf{F}_{adh,x}^p - r_x \mathbf{F}_{adh,z}^p) - \frac{1}{I} \sum_U (r_{U,z} \bar{\rho}_U \mathbf{u}_{U,x} - r_{U,x} \bar{\rho}_U \mathbf{u}_{U,z}) + \frac{1}{I} \sum_C (r_{C,z} \rho_C \mathbf{u}_{C,x} - r_{C,x} \rho_C \mathbf{u}_{C,z}), \quad (\text{A28})$$

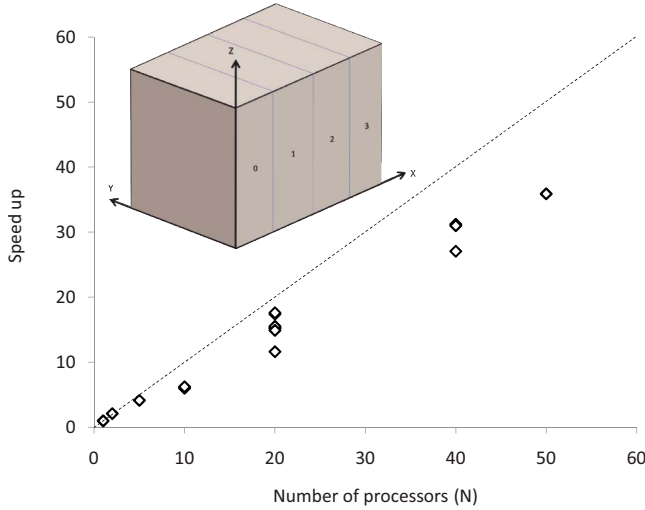


FIG. 12. (Color online) Comparison of the actual speed up (data points) obtained using the parallel LBM with the ideal or linear speed-up (dashed line). The inset shows how the 3D solution domain is split into equal volume slices along x . LBM calculations in each slice are performed in parallel by different processors. Data communication between adjacent processors takes place across the surface area perpendicular to the x axis. This schematic shows a case with four processors are being used.

$$\begin{aligned}
 B_6 = & \Omega_{z,0} + \frac{2}{I} \sum_{bn} \sum_{\alpha} (r_x f_{\alpha}^+ e_{\alpha y} - r_y f_{\alpha}^+ e_{\alpha x}) \\
 & + \frac{1}{I} \sum_{bn} (r_x \mathbf{F}_{adh,y}^p - r_y \mathbf{F}_{adh,x}^p) \\
 & - \frac{1}{I} \sum_U (r_{U,x} \bar{\rho}_U \mathbf{u}_{U,y} - r_{U,y} \bar{\rho}_U \mathbf{u}_{U,x}) \\
 & + \frac{1}{I} \sum_C (r_{C,x} \rho_C \mathbf{u}_{C,y} - r_{C,y} \rho_C \mathbf{u}_{C,x}). \quad (A29)
 \end{aligned}$$

In the above expressions, the subscript 0 represents (known) values of the particle velocities at the current time level. The summations are to be carried out over each boundary node (bn) and over all the relevant directions (α) at that boundary node. The location of the relevant node point on the particle surface, relative to the particle center, is denoted by (r_x, r_y, r_z) . The lubrication force between particle pairs does not contribute to the torque and is dealt with in an explicit manner, using the relative velocity between the particle pairs from the current time level. Likewise, the Hookean force between particle pairs does not contribute to the rotational

dynamics and, in addition, is independent of the relative velocity between the pair of particles. Implementing this scheme requires two passes through the domain. During the first pass, the coefficients A_{ij} and B_i are assembled. After the linear system of equations, i.e., Eq. (A2) is solved, another pass through the domain is made to update the relevant PDFs based on the calculated values. Expressions for the adhesive forces and the forces because of changing particle representation on the lattice in B_i can be found in Ref. [67]. The advantage of using the implicit scheme is that rotational dynamics can be included in the calculations without introducing numerical instability. The scheme described here can be implemented for any number of suspended particles as long as the particles do not penetrate each another.

APPENDIX B: PARALLEL IMPLEMENTATION OF THE LBM

The 3D LBM model was implemented in FORTRAN 90 using the message passing interface (MPI) library. A 1D domain decomposition along the x axis was used for simplicity (inset in Fig. 12). The typical run-time for a $201 \times 201 \times 101$ lattice using 20 processors was approximately 1 h per 1000 lattice time steps. Parallel performance of the LBM can be quantified by running the same simulation with different number of processors and calculating the ratio of the computational time required for a single processor with the computational time required using N processors, which is called the speed-up. Ideally, if N processors are used, the computation time should reduce by a factor of N , but in practice, this type of linear speed-up is not obtained because of the time spent in communicating information between adjacent processors. The actual speed-up plot for the present LBM is shown in Fig. 12, where data points represent LBM results and the dashed line indicates the ideal or linear speed-up.

It can be seen that parallel efficiency, defined as the ratio of actual to ideal speed-up reduces as the number of processors are increased. However, using more processors is still useful because of the large reduction in computational time, especially for large lattice sizes. In the present work, we used up to 50 processors, which was quite sufficient for the lattice sizes considered here. Additional computational overheads can be eliminated if the suspended particles are also treated in parallel along with the fluid flow. At present, each processor store data for all particles, irrespective of whether the particle actually resides in the specific portion of the domain handled by the processor or not. Thus, the parallel efficiency reduces if more particles are used. For a more detailed discussion about how the particle dynamics can be parallelized, the reader is referred to Stratford and Pagonabarraga [66].

- [1] D. Bonn, J. Eggers, and J. Indekeu, *Rev. Mod. Phys.* **81**, 739 (2009).
 [2] F. T. Dodge, *J. Colloid Interface Sci.* **121**, 154 (1988).
 [3] A. Zosel, *Colloid Polym. Sci.* **271**, 680 (1993).
 [4] Y. Gu and D. Li, *Colloids Surf., A* **142**, 243 (1998).

- [5] Y. Gu and D. Li, *Colloids Surf., A* **163**, 239 (2000).
 [6] E. Bertrand, T. D. Blake, and J. D. Coninck, *J. Phys.: Condens. Matter* **21**, 464124 (2009).
 [7] S. Mukherjee and J. Abraham, *J. Colloid Interface Sci.* **312**, 341 (2007).

- [8] M. Elimelech, J. Gregory, X. Jia, and R. A. Williams, *Particle Deposition and Aggregation: Measurement, Modelling and Simulation* (Butterworth-Heinemann, London, 1995).
- [9] B. V. Deryaguin and L. Landau, *Acta Chem. Scand.*, Ser. A **14**, 633 (1941).
- [10] B. V. Deryaguin and L. Landau, *Sov. Phys. JETP* **15**, 633 (1945).
- [11] E. J. W. Verwey and J. T. G. Overbeek, *Theory of the Stability of Lyophobic Colloids* (Elsevier, Amsterdam, 1948).
- [12] M. Nicolas, *J. Fluid Mech.* **545**, 271 (2005).
- [13] H. J. Jeong, W. R. Hwang, C. Kim, and S. J. Kim, *J. Mater. Process. Technol.* **210**, 297 (2010).
- [14] E. Tekin, P. J. Smith, and U. S. Schubert, *Soft Matter* **4**, 703 (2008).
- [15] H. Dong, W. W. Carr, and J. F. Morris, *Rev. Sci. Instrum.* **77**, 085101 (2006).
- [16] R. D. Deegan, O. Bakajin, T. F. Dupant, G. Huber, S. R. Nagel, and T. A. Witten, *Nature (London)* **389**, 827 (1997).
- [17] R. D. Deegan, *Phys. Rev. E* **61**, 475 (2000).
- [18] R. D. Deegan, O. Bakajin, T. F. Dupont, G. Huber, S. R. Nagel, and T. A. Witten, *Phys. Rev. E* **62**, 756 (2000).
- [19] H. Hu and R. G. Larson, *J. Phys. Chem. Lett.* **110**, 7090 (2006).
- [20] G. D. Nadkarni and S. Garoff, *EPL* **20**, 523 (1992).
- [21] S. Herminghaus, M. Brinkmann, and R. Seemann, *Annu. Rev. Mater. Sci.* **38**, 101 (2008).
- [22] J. H. Kim, S. I. Ahn, J. H. Kim, and W. C. Zin, *Langmuir* **23**, 6163 (2007).
- [23] J. Perelaer, P. J. Smith, C. E. Hendriks, A. M. J. van den Berg, and U. S. Schubert, *Soft Matter* **4**, 1072 (2008).
- [24] J. Park and J. Moon, *Langmuir* **22**, 3506 (2006).
- [25] D. M. Kuncicky and O. D. Velev, *Langmuir* **24**, 1371 (2008).
- [26] E. Widjaja and M. T. Harris, *AIChE J.* **54**, 2250 (2008).
- [27] R. Bhardwaj, X. Fang, and D. Attinger, *New J. Phys.* **11**, 075020 (2009).
- [28] R. Bhardwaj, X. Fang, P. Somasundaran, and D. Attinger, *Langmuir* **26**, 7833 (2010).
- [29] A. S. Joshi and Y. Sun, *J. Disp. Technol.* (to be published).
- [30] S. Biswas, S. Gawande, V. Bromberg, and Y. Sun, *ASME J. Sol. Energy Eng.* **132**, 021010 (2010).
- [31] R. J. Furbank and J. F. Morris, *Phys. Fluids* **16**, 1777 (2004).
- [32] D. Leighton and A. Acrivos, *Chem. Eng. Sci.* **41**, 1377 (1986).
- [33] A. M. Morales, R. Pitchumani, T. J. Garino, A. K. Gutmann, and L. A. Domeier, *J. Am. Ceram. Soc.* **88**, 570 (2005).
- [34] A. Mawardi, Y. Xiao, and R. Pitchumani, *Int. J. Multiphase Flow* **34**, 227 (2008).
- [35] R. Yang, D. C. Sun, and S. Park, *J. Electron. Mater.* **35**, 2016 (2006).
- [36] R. Yang, D. C. Sun, and S. Park, *J. Electron. Mater.* **35**, 2026 (2006).
- [37] N. Huang, G. Ovarlez, F. Bertrand, S. Rodts, P. Coussot, and D. Bonn, *Phys. Rev. Lett.* **94**, 028301 (2005).
- [38] J. F. Brady and G. Bossis, *Annu. Rev. Fluid Mech.* **20**, 111 (1988).
- [39] A. Perrin and H. H. Hu, *J. Comput. Phys.* **212**, 166 (2006).
- [40] A. Perrin and H. H. Hu, *J. Comput. Phys.* **227**, 8776 (2008).
- [41] A. A. Mammoli and M. S. Ingber, *Eng. Anal. Boundary Elem.* **24**, 65 (2000).
- [42] M. S. Ingber, S. Feng, A. L. Graham, and H. Brenner, *J. Fluid Mech.* **598**, 267 (2008).
- [43] W. R. Hwang, M. A. Hulsen, and H. E. H. Meijer, *J. Comput. Phys.* **194**, 742 (2004).
- [44] W. R. Hwang, M. A. Hulsen, and H. E. H. Meijer, *J. Non-Newtonian Fluid Mech.* **121**, 15 (2003).
- [45] A. J. C. Ladd, *J. Fluid Mech.* **271**, 285 (1994).
- [46] A. J. C. Ladd, *J. Fluid Mech.* **271**, 311 (1994).
- [47] A. J. C. Ladd and R. Verberg, *J. Stat. Phys.* **104**, 1191 (2001).
- [48] N. Q. Nguyen and A. J. C. Ladd, *Phys. Rev. E* **66**, 046708 (2002).
- [49] B. Chun and A. J. C. Ladd, *Phys. Rev. E* **75**, 066705 (2007).
- [50] C. K. Aidun, Y. Lu, and E. J. Ding, *J. Fluid Mech.* **373**, 287 (1998).
- [51] E. J. Ding and C. K. Aidun, *J. Stat. Phys.* **112**, 685 (2003).
- [52] M. W. Heemels, M. H. J. Hagen, and C. P. Lowe, *J. Comput. Phys.* **164**, 48 (2000).
- [53] C. P. Lowe, D. Frenkel, and A. J. Masters, *J. Chem. Phys.* **103**, 1582 (1995).
- [54] A. K. Gunstensen, D. H. Rothman, S. Zaleski, and G. Zanetti, *Phys. Rev. A* **43**, 4320 (1991).
- [55] X. Shan and H. Chen, *Phys. Rev. E* **47**, 1815 (1993).
- [56] X. Shan and H. Chen, *Phys. Rev. E* **49**, 2941 (1994).
- [57] M. R. Swift, W. R. Osborn, and J. M. Yeomans, *Phys. Rev. Lett.* **75**, 830 (1995).
- [58] M. R. Swift, E. Orlandini, W. R. Osborn, and J. M. Yeomans, *Phys. Rev. E* **54**, 5041 (1996).
- [59] X. Shan, *Phys. Rev. E* **73**, 047701 (2006).
- [60] H. Kusumaatmaja, R. J. Vrancken, C. W. M. Bastiaansen, and J. M. Yeomans, *Langmuir* **24**, 7299 (2008).
- [61] A. Dupuis and J. M. Yeomans, *FGCS, Future Gener. Comput. Syst.* **20**, 993 (2004).
- [62] A. Dupuis and J. M. Yeomans, *Langmuir* **21**, 2624 (2005).
- [63] J. M. Yeomans and H. Kusumaatmaja, *Bull. Pol. Acad. Sci.* **55**, 203 (2007).
- [64] K. Stratford, R. Adhikari, I. Pagonabarraga, and J. C. Desplat, *J. Stat. Phys.* **121**, 163 (2005).
- [65] K. Stratford, R. Adhikari, I. Pagonabarraga, J. C. Desplat, and M. E. Cates, *Science* **309**, 2198 (2005).
- [66] K. Stratford and I. Pagonabarraga, *Comput. Math. Appl.* **55**, 1585 (2008).
- [67] A. S. Joshi and Y. Sun, *Phys. Rev. E* **79**, 066703 (2009).
- [68] J. Onishi, A. Kawasaki, Y. Chen, and H. Ohashi, *Comput. Math. Appl.* **55**, 1541 (2008).
- [69] A. L. Kupershtokh and D. A. Medvedev, *J. Electrostat.* **64**, 581 (2006).
- [70] J. F. Brady and G. Bossis, *J. Fluid Mech.* **155**, 105 (1985).
- [71] G. Bossis and J. F. Brady, *J. Chem. Phys.* **87**, 5437 (1987).
- [72] G. Bossis, A. Meunier, and J. D. Sherwood, *Chem. Eng. Sci.* **47**, 981 (1992).
- [73] J. Hyvaluoma, P. Raiskinmaki, A. Koponen, M. Kataja, and J. Timonen, *J. Stat. Phys.* **121**, 149 (2005).
- [74] J. Kromkamp, D. V. den Ende, D. Kandhai, R. van der Sman, and R. Boom, *Chem. Eng. Sci.* **61**, 858 (2006).
- [75] M. E. Cates, K. Stratford, R. Adhikari, P. Stansell, J. C. Desplat, I. Pagonabarraga, and A. J. Wagner, *J. Phys.: Condens. Matter* **16**, S3903 (2004).
- [76] E. Kim, K. Stratford, P. J. Camp, and M. E. Cates, *J. Phys. Chem. B* **113**, 3681 (2009).
- [77] H. Basagaoglu and S. Succi, *J. Chem. Phys.* **132**, 134111 (2010).
- [78] H. Kusumaatmaja and J. M. Yeomans, *Langmuir* **23**, 6019

- (2007).
- [79] A. L. Yarin, *Annu. Rev. Fluid Mech.* **38**, 159 (2006).
- [80] J. J. Stickel and R. L. Powell, *Annu. Rev. Fluid Mech.* **37**, 129 (2005).
- [81] S. Sikalo, H. D. Wilhelm, I. V. Roisman, S. Jakirlic, and C. Tropea, *Phys. Fluids* **17**, 062103 (2005).
- [82] A. Einstein, *Ann. Phys.* **19**, 289 (1906).
- [83] I. M. Krieger and T. Dougherty, *Trans. Soc. Rheol.* **3**, 137 (1959).
- [84] S. Torquato, T. M. Truskett, and P. G. Debenedetti, *Phys. Rev. Lett.* **84**, 2064 (2000).
- [85] L. Dong and D. T. Johnson, *Adv. Space Res.* **32**, 149 (2003).
- [86] L. Dong and D. T. Johnson, *J. Dispersion Sci. Technol.* **25**, 575 (2004).
- [87] E. Vignati and R. Piazza, *Langmuir* **19**, 6650 (2003).
- [88] T. N. Hunter, R. J. Pugh, G. V. Franks, and G. J. Jameson, *Adv. Colloid Interface Sci.* **137**, 57 (2008).
- [89] T. Lee and C.-L. Lin, *Phys. Rev. E* **67**, 056703 (2003).
- [90] K. S. Birdi, D. T. Vu, and A. Winter, *J. Phys. Chem.* **93**, 3702 (1989).
- [91] C. B. Monnier and M. E. R. Shanahan, *Langmuir* **11**, 2820 (1995).
- [92] M. L. Turner, L. Knüfing, C. H. Arns, A. Sakellariou, T. J. Senden, A. P. Sheppard, R. M. Sok, A. Limaye, W. V. Pinczewski, and M. A. Knackstedt, *Physica A* **339**, 166 (2004).
- [93] D. J. Norris, E. G. Arlinghaus, L. Meng, R. Heiny, and L. E. Scriven, *Adv. Mater.* **16**, 1393 (2004).